

# A density functional theory study on the mechanism of the allylpalladium-catalyzed dehydrogenation of aldehydes and cyclic ketones

Progress in Reaction Kinetics  
and Mechanism

Volume 46: 1–14

© The Author(s) 2021

Article reuse guidelines:

sagepub.com/journals-permissions

DOI: 10.1177/14686783211020600

journals.sagepub.com/home/prk

Anan Haj Ichia Arisha<sup>1,2</sup>

## Abstract

The results of density functional theory calculations at the APFD/SDD level are detailed herein in order to study the main steps in the  $\alpha,\beta$ -dehydrogenation of aldehydes and cyclic ketones in the presence of an allylpalladium complex catalyst. The mechanism is believed to proceed via an allylpalladium enolate complex (**A**) in equilibrium with the carbon-bonded complex (**B**), followed by  $\beta$ -hydride elimination to yield the allylpalladium hydride coordinated to the  $\alpha,\beta$ -unsaturated carbonyl (complex **C**). The optimized structures and detailed energy profiles of these intermediates and their corresponding transition states are presented herein. The results indicate that the intermediates and their transition states are more stable in THF solution than in the gas phase. In detail, the energy barriers for the two steps are found to be 25.22 and 11.13 kcal/mol, respectively, in THF, and 29.93 and 9.77 kcal/mol, respectively, in the gas phase.

## Keywords

density functional theory, allylpalladium, dehydrogenation,  $\alpha$ ,  $\beta$ -unsaturated carbonyl,  $\beta$ -elimination

<sup>1</sup>Department of Organic Chemistry, School of Chemistry, Faculty of Exact Sciences, Tel Aviv University, Tel Aviv, Israel

<sup>2</sup>Department of Education, Beit Berl College, Beit Berl, Israel

## Corresponding author:

Anan Haj Ichia Arisha, Department of Organic Chemistry, School of Chemistry, Faculty of Exact Sciences, Tel Aviv University, Tel Aviv 6997801, Israel.

Email: ananaris@zahav.net.il



Creative Commons Non Commercial CC BY-NC: This article is distributed under the terms of the Creative Commons Attribution-NonCommercial 4.0 License (<https://creativecommons.org/licenses/by-nc/4.0/>) which permits non-commercial use, reproduction and distribution of the work without further permission provided the original work is attributed as specified on the SAGE and Open Access pages (<https://us.sagepub.com/en-us/nam/open-access-at-sage>).

## Introduction

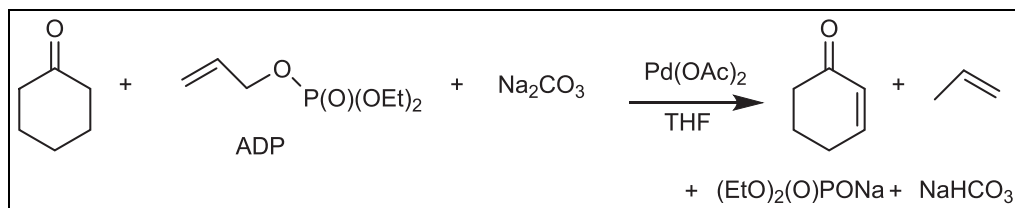
The conversion of saturated ketones and aldehydes to the corresponding  $\alpha,\beta$ -unsaturated compounds is an important synthetic tool. In particular, the introduction of a double bond in the  $\alpha,\beta$  position is of great interest, because this bond can be subsequently modified to provide a wide range of functional groups, thus potentially opening up an easy route to the synthesis of many organic compounds. Between 1982 and 1983, Shimizu and colleagues<sup>1–5</sup> reported a methodology for the regioselective dehydrogenation of carbonyl compounds in the presence of an allylpalladium catalyst. Two competitive reactions—namely, allylation and dehydrogenation—were identified and controlled by adjustment of the specific ligand, solvent, and temperature. For instance, acetonitrile at 80°C was found to be the most suitable solvent for the dehydrogenation pathway. In addition, the molar ratio of the palladium and phosphine ligand was found to be crucial, with the dehydrogenation proceeding efficiently at a ratio of less than two, or even in the absence of the phosphine ligand. With respect to the choice of ligand, 1,2-bis(diphenylphosphino)ethane (dppe) was found to be the best choice for obtaining the dehydrogenation product.

More recently (in 2010), Muzart<sup>6</sup> published a detailed review on the preparation of  $\alpha,\beta$ -unsaturated carbonyls from the corresponding saturated compounds and palladium reagents, with both stoichiometric and catalytic methods being explained. Furthermore, in 2018, Huang et al.<sup>7</sup> developed a method for synthesizing  $\alpha,\beta$ -unsaturated cyclic ketones from the zinc enolate derivatives.

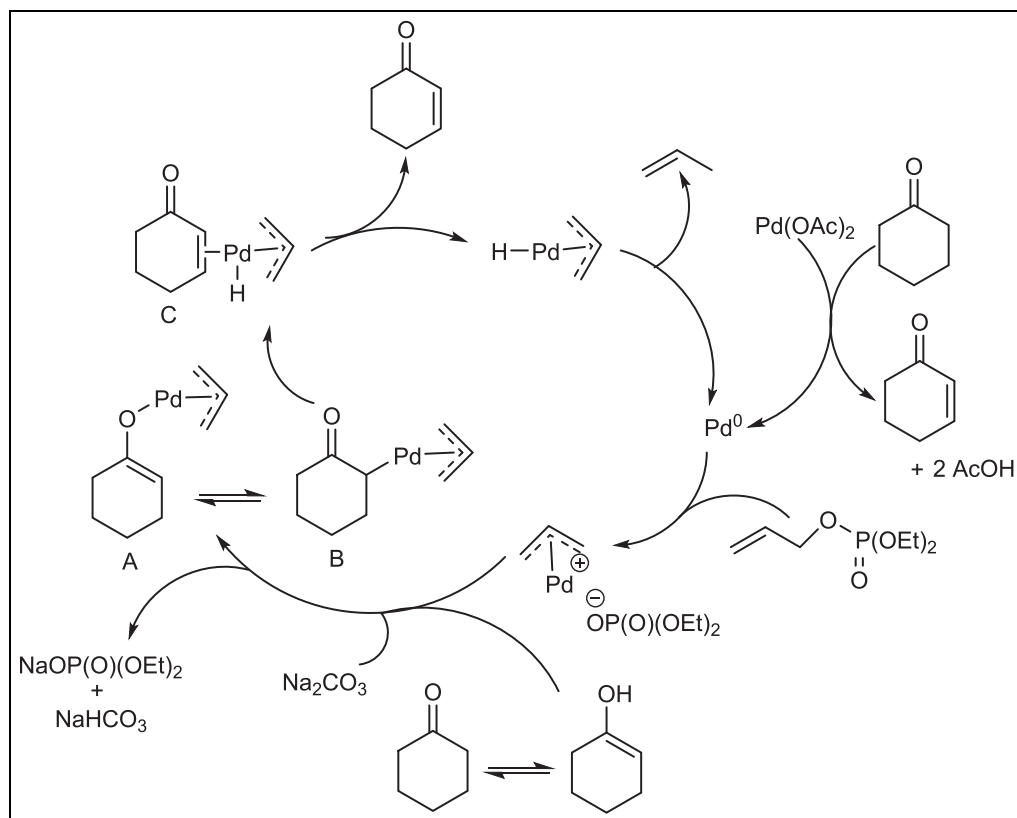
A great deal of recent development has been reported in the use of manganese as a cheap and environmentally friendly catalyst for hydrogenation and dehydrogenation reactions.<sup>8</sup> In addition, Maiti et al. have reported the use of a cobalt catalyst to introduce an internal aliphatic olefin during the Heck-type dehydrogenation reaction,<sup>9–11</sup> and palladium catalysis for the selective C–H allylation of arenes.<sup>12,13</sup> Furthermore, Mishra et al.<sup>14</sup> have published a detailed review of the catalytic allylation of  $C(sp^2)$ –H bonds with various transition metal catalysts.

A new route for the preparation of  $\alpha,\beta$ -unsaturated aldehydes and cyclic ketones in the presence allyl diethyl phosphate (ADP), THF and  $Na_2CO_3$ , and a palladium catalyst, without using any ligand, has been developed by the present research group.<sup>15</sup> The overall reaction is shown in Scheme 1.

A reasonable mechanism is outlined in Scheme 2. Thus, the reduction of  $Pd(OAc)_2$  with cyclohexanone gives  $Pd^0$  as the actual catalyst, and the  $\eta^3$ -allylpalladium cation is formed in the presence of allyl phosphate. Under basic conditions, enolate is present and reacts with the allylpalladium to give complex **A**, which is in equilibrium with complex **B**. Next,



**Scheme 1.** The dehydrogenation of cyclohexanone.



**Scheme 2.** A plausible reaction mechanism for the dehydrogenation of cyclohexanone.

the  $\beta$ -hydride elimination of **B** affords complex **C**, which evolves the final product, cyclohex-2-en-1-one. Meanwhile, propene is formed via reductive elimination of the allylpalladium hydride, and the  $\text{Pd}^0$  catalyst is regenerated.

In a versatile computational study on the Tsuji allylation reaction, Keith et al.<sup>16</sup> showed that the observed enantioselectivity in the Pd-catalyzed intramolecular decarboxylative allylic alkylation of allyl enol carbonates is best explained by an inner-sphere pathway. However, to the best of the present authors' knowledge, no extensive computational studies have been performed on the dehydrogenation reaction in the presence of allylpalladium catalysts. Herein, a computational density functional theory (DFT) investigation of the optimized structures of complexes **A**, **B**, and **C** and the corresponding transition states  $\text{TS}_{\text{AB}}$  and  $\text{TS}_{\text{BC}}$  (Scheme 2) is presented.

## Computational methods

All DFT calculations were performed using the Gaussian 16 software<sup>17</sup> supported by the GaussView 6.0 interface.<sup>18</sup> All geometric optimizations and frequency calculations were performed using the APF-D hybrid DFT method including dispersion (keyword APFD) with

the SDD basis set. For higher accuracy, the ultrafine grid was used and was specified by the `Int = Ultrafine` keyword. Frequency calculations were also performed at the same level of theory to identify all of the stationary points as minima (zero imaginary frequencies) or transition states (one imaginary frequency). The transition states were optimized via the synchronous transit-guided quasi-Newton methods (QST2 and QST3). Intrinsic reaction coordinate (IRC) calculations were performed at the same level to verify that the transition states led to the expected reactants and products. Moreover, the calculation with THF as the solvent was accomplished by adding the self-consistent reaction field as `SCRF = (SMD, solvent = THF)`. The discussions herein are based on the Gibbs energies, with the difference in Gibbs energy between the reactant and transition state being used to calculate the energy barrier. All reported energy values refer to the standard conditions, that is, 298.15 K and 1 atm pressure. The calculated imaginary frequencies of all transition-state species, along with the Cartesian coordinates and thermodynamic parameters of all the calculated structures, are provided in the Supplementary Material.

## Results and discussion

The optimized geometry of complex **A** in the gas phase is presented in Figure 1, and the selected bond lengths are given in Table 1.

Complex **A** is a Pd(II),  $d^8$ , 16 e complex, which is stabilized by bonding to  $\pi$ -allyl and oxo- $\pi$ -allyl systems. The lengths of the C2–C4 (1.447), C4–C5 (1.408), and C6–C8 (1.429 Å) bonds are between that of a typical C–C single bond (1.54 Å) and that of a C = C double bond (1.33 Å), corresponding to the  $\pi$ -allyl moiety. Similarly, the length of the O3–C6 (1.329 Å) bond is between that of a single C–O bond (1.43 Å) and that of a C = O double bond (1.20 Å), thus indicating enolate ion coordination. The bonding of Pd to C8 may enhance the  $\beta$ -elimination process by positioning the palladium close to H16. However, this proximity could be disturbed by the presence of ligands. The Gibbs energy and the relative Gibbs energies in the gas phase are given in Table 2, and those in THF are listed in Table 3.

These results indicate that complex **A** is stabilized in the presence of THF by 10.42 kcal/mol, which indicates a charge distribution in this complex. Indeed, all the intermediates and the transition states are more stable in THF than in the gas phase.

The optimized geometry of complex **B** in the gas phase is shown in Figure 2, and the selected bond lengths are given in Table 4.

Complex **B** is a Pd(II), 14 e complex, which bonds strongly to C5 and C8 (2.062 Å) and less strongly to the C2–C4  $\pi$  system (Pd1–C2 = 2.462 Å and Pd1–C4 = 2.283 Å). In contrast to complex **A**, complex **B** has no enolate coordination, while the C6–C8 bond is longer (1.476 Å) and the O3–C6 bond (1.262 Å) is shorter. Hence, complex **A** is more stable than complex **B**, the former being less energetic by 9.42 kcal/mol in the gas phase and by 6.97 kcal/mol in THF. In complex **B**, the palladium is in the correct position for  $\beta$ -elimination, and the Pd1–H16 distance is 2.918 Å.

The calculated optimized structure of the transition state between complex **A** and complex **B** (designated **TS<sub>AB</sub>**) in the gas phase is shown in Figure 3, and the relevant interatomic distances are given in Table 5. These results reveal the movement of C5 toward palladium, with a Pd1–C5 bond length of 2.069 Å compared to that of 2.342 Å in complex **A**. Furthermore, the distance between C2 and palladium has increased to 2.282 Å in **TS<sub>AB</sub>** compared to 2.102 Å in complex **A**. In addition, a movement of palladium toward C8, and a

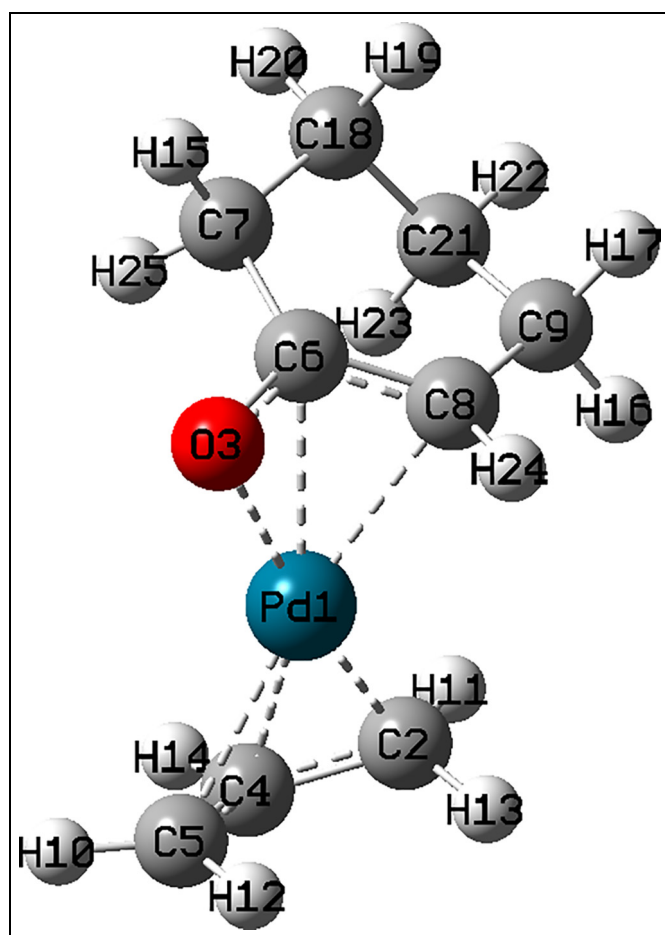


**Figure 1.** The optimized structure of complex **A**.

**Table 1.** Selected bond lengths for complex **A** (Å).

Bond	Length
Pd1–C2	2.102
Pd1–C4	2.237
Pd1–C5	2.342
Pd1–C6	2.326
Pd1–C8	2.270
Pd1–O3	2.225
C2–C4	1.447
C4–C5	1.408
C6–C8	1.429
O3–C6	1.329

**Table 2.** The Gibbs energy and the relative Gibbs energies of **A**, **B**, **C**, **TS<sub>AB</sub>**, and **TS<sub>BC</sub>** in the gas phase.

Species	Gibbs energy (Hartree)	Relative Gibbs energy (kcal/mol)
Complex <b>A</b>	−553.967191	0.00
Complex <b>B</b>	−553.952184	9.42
<b>TS<sub>AB</sub></b>	−553.919496	29.9
Complex <b>C</b>	−553.947885	12.1
<b>TS<sub>BC</sub></b>	−553.936614	19.2

**Table 3.** The Gibbs energy and the relative Gibbs energies of **A**, **B**, **C**, **TS<sub>AB</sub>**, and **TS<sub>BC</sub>** in THF.

Species	Gibbs energy (Hartree)	Relative Gibbs energy (kcal/mol)
Complex <b>A</b>	−553.983797	0.00
Complex <b>B</b>	−553.972695	6.97
<b>TS<sub>AB</sub></b>	−553.943613	25.2
Complex <b>C</b>	−553.965898	11.2
<b>TS<sub>BC</sub></b>	−553.954958	18.1

disconnection from oxygen, are observed, with an increase in the Pd1–O3 distance from 2.225 Å in complex **A** to 2.775 Å in **TS<sub>AB</sub>**. Meanwhile, the O3–C6 bond length is decreased from 1.329 Å in complex **A** to 1.302 Å in **TS<sub>AB</sub>**, and the C6–C8 bond length is increased from 1.429 to 1.444 Å, thus approaching the keto form.

The results in Tables 2 and 3 indicate that the transition state, **TS<sub>AB</sub>**, is stabilized by 15.13 kcal/mol when the reaction is performed in THF as solvent rather than in the gas phase. This is in accordance with the well-known fact that the aprotic solvents are the best choice for the dehydrogenation reaction. Moreover, a comparison of the Gibbs energy profiles in Figures 4 and 5 indicates that the energy barrier between complexes **A** and **B** is higher in the gas phase (29.93 kcal/mol) than in THF (25.22 kcal/mol), thus further demonstrating the greater stability of the transition state in the THF phase.

As the reaction continues, complex **C** is obtained via β-elimination of complex **B**. The optimized structure of complex **C** is shown in Figure 6, and the selected interatomic distances are presented in Table 6.

Complex **C** is a Pd(II), d<sup>8</sup>, 16 e complex in which the palladium atom is bonded to both C8 and C9; so that the Pd1–C5 bond length is increased to 2.385 Å (compared to 2.062 Å in **B**), and the Pd1–C2 bond length is decreased to 2.213 Å (compared to 2.462 Å in **B**). Meanwhile, the Pd1–C8 bond length is increased from 2.062 in **B** to 2.284 Å in **C**, and the Pd1–C9 bond (which is absent in **B**) has a length of 2.306 Å. In addition, a double bond is formed between C8 and C9 in complex **C**, with a C8 = C9 bond length of 1.404 Å compared to the C8–C9 single-bond length of 1.529 Å in complex **B**. Moreover, complex **C** is a palladium hydride complex with a Pd–H bond length of 1.582 Å, which can liberate cyclohex-2-enone as the final dehydrogenation product.

The optimized structure of the transition state between complexes **B** and **C** (designated **TS<sub>BC</sub>**) is presented in Figure 7, and the selected interatomic distances are listed in Table 7. Here, the C6–C8 length is seen to be 1.450 Å, which is in between the 1.529 Å of **B** and the

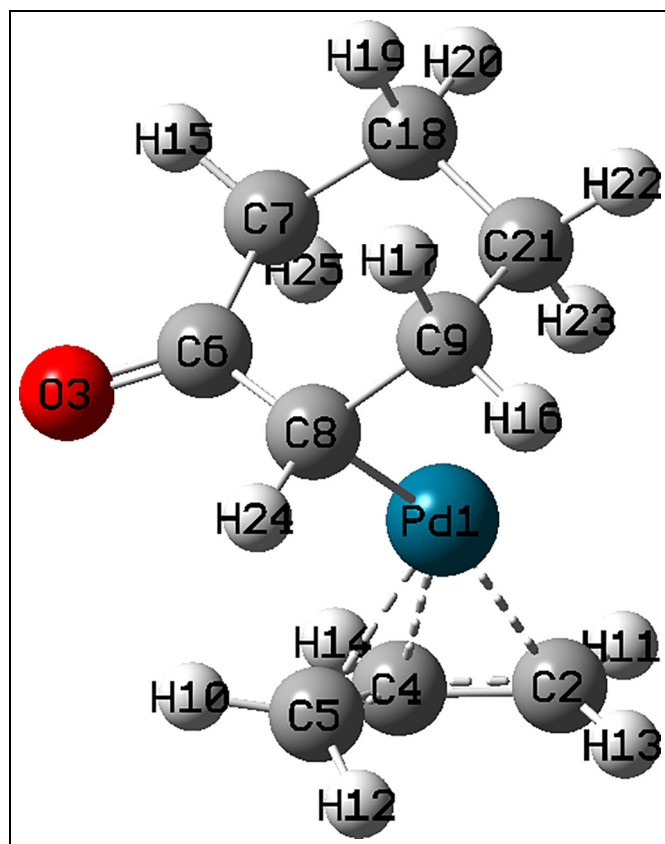


**Figure 2.** The optimized structure of complex **B**.

**Table 4.** Selected bond lengths for complex **B** (Å).

Bond	Length
PdI–C2	2.462
PdI–C4	2.283
PdI–C5	2.062
PdI–C8	2.062
PdI–C9	2.691
PdI–H16	2.918
C9–H16	1.097
C2–C4	1.392
C4–C5	1.461
C5–C8	3.173
C6–C8	1.476
C8–C9	1.529
O3–C6	1.262

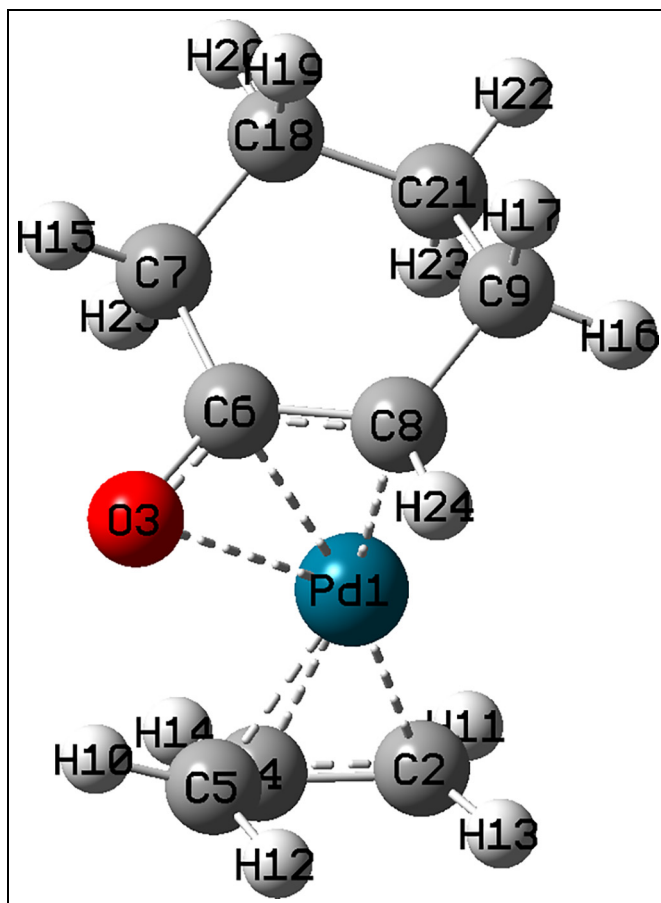


**Figure 3.** The optimized structure of  $\text{TS}_{\text{AB}}$ .

1.483 Å of **C**, thus demonstrating the formation of the double bond. Moreover, the C9–H16 bond length is increased from 1.097 Å in **B** to 1.642 Å in  $\text{TS}_{\text{BC}}$ , thus indicating the abstraction of H16 by palladium. The resulting four-center transition state (Pd1, C8, C9, and H16) is suitable for the  $\beta$ -hydride elimination mechanism. As indicated in Figures 4 and 5, the energy barrier between **B** and **C** is lower than that between **A** and **B**. Moreover, in THF, complex **B** is stabilized by 12.87 kcal/mol, and  $\text{TS}_{\text{BC}}$  is stabilized by 11.51 kcal/mol. Hence, the energy barrier between **B** and **C** is 9.77 kcal/mol in the gas phase, which is lower by 1.36 kcal/mol than that in THF (11.13 kcal/mol). However, as noted above, the transformation from **A** to **B** is slower and is thus the rate-determining step.

To confirm the proposed mechanism, the electrostatic potential map of the  $\text{TS}_{\text{BC}}$  is presented in Figure 8.

Here, it can be seen that H16 is more negative than H17, thus indicating the movement of H16 away from carbon and toward the Pd (i.e. a hydride transfer). Moreover, the highest occupied molecular orbital (HOMO) and the lowest unoccupied molecular orbital (LUMO) of complex **B** are shown in Figures 9 and 10, respectively, where the energy difference of



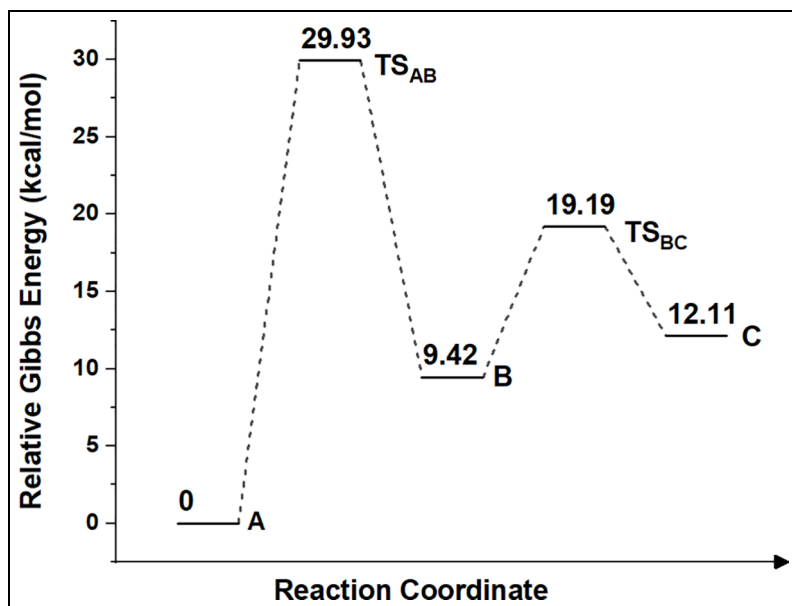


**Figure 4.** The relative Gibbs energy changes during the reaction in the gas phase.

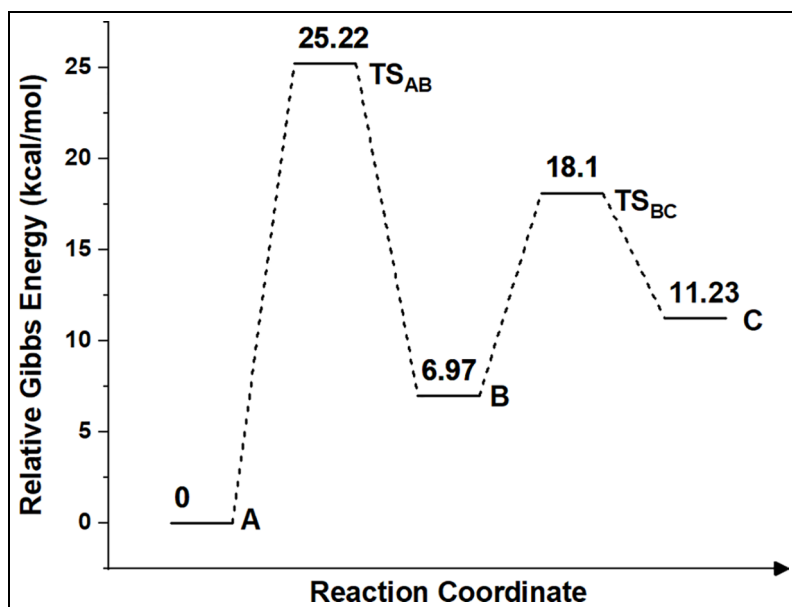


**Figure 5.** The relative Gibbs energy changes during the reaction in THF.

**Table 5.** Selected bond lengths for **TS<sub>AB</sub>** (Å).

Bond	Length
PdI–C2	2.282
PdI–C4	2.224
PdI–C5	2.069
PdI–C6	2.432
PdI–C8	2.273
PdI–O3	2.775
C2–C4	1.416
C4–C5	1.445
C6–C8	1.444
O3–C6	1.302

**Table 6.** Selected bond lengths for complex **C** (Å).

Bond	Length
PdI–C2	2.213
PdI–C4	2.293
PdI–C5	2.385
PdI–C8	2.284
PdI–C9	2.306
PdI–H16	1.582
C2–C4	1.442
C4–C5	1.404
C8–C9	1.404
C6–C8	1.483
O3–C6	1.254

3.92 eV between them clearly allows for electron transfer from the HOMO to the LUMO. Furthermore, the lobe in the HOMO around H16 can easily interact with that in the LUMO around Pd and C8, which is the key interaction leading to the formation of complex **C**.

## Conclusion

Herein, DFT calculations at the APFD/SDD level were performed in order to study the key steps in the mechanism of the  $\alpha,\beta$ -dehydrogenation reaction of aldehydes and cyclic ketones catalyzed by an allylpalladium complex. The intermediates in this reaction (structures **A**, **B**, and **C**) and the corresponding transition states (**TS<sub>AB</sub>** and **TS<sub>BC</sub>**) were optimized. Moreover, these intermediates and transition states were shown to be more stable in THF than in the gas phase. The energy barrier between **A** and **B** was found to be 25.22 kcal/mol in THF compared to 29.93 kcal/mol in the gas phase. Meanwhile, the energy barrier between **B** and **C** was 11.13 kcal/mol in THF compared to 9.77 kcal/mol in the gas phase, thus demonstrating that THF is a suitable solvent for this reaction. It is anticipated that the results of this study

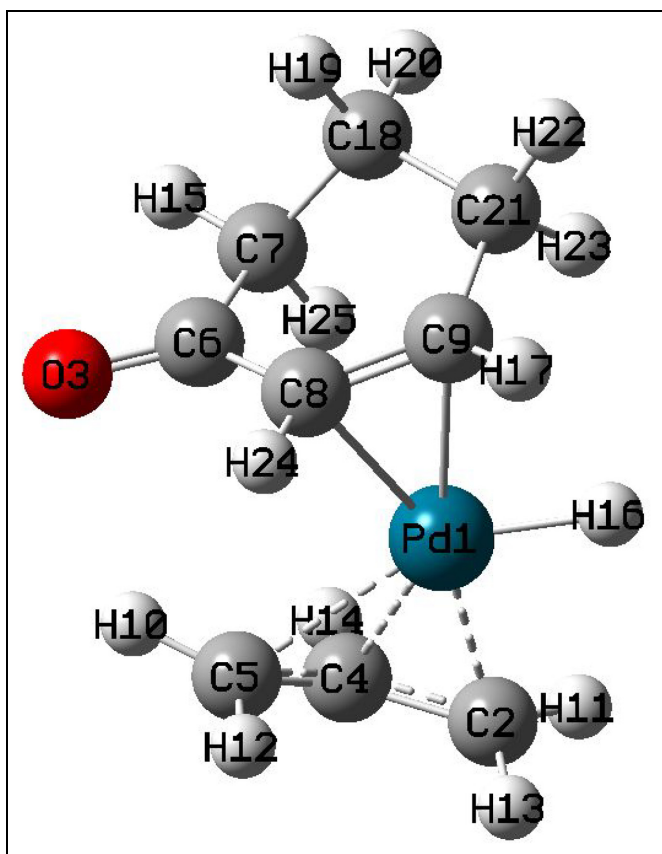


**Figure 6.** The optimized structure of complex **C**.

**Table 7.** Selected bond lengths for **TS<sub>BC</sub>** (Å).

Bond	Length
Pd1–C2	2.284
Pd1–C4	2.263
Pd1–C5	2.289
Pd1–C8	2.131
Pd1–C9	2.272
Pd1–H16	1.630
C9–H16	1.642
C2–C4	1.427
C4–C5	1.421
C8–C9	1.450
C6–C8	1.473
O3–C6	1.257

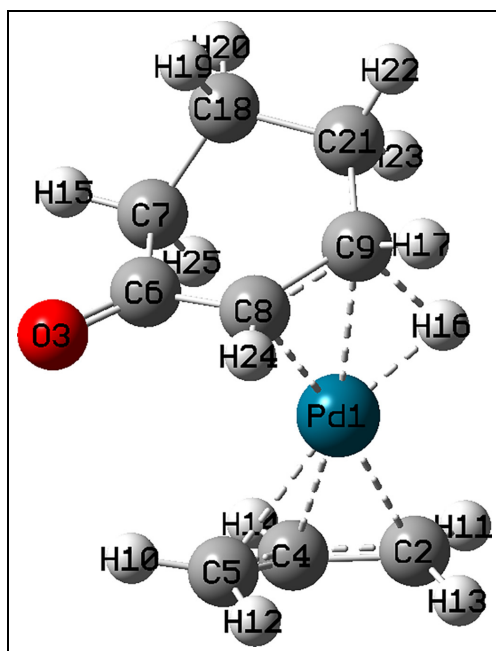


**Figure 7.** The optimized structure of **TS<sub>BC</sub>**.

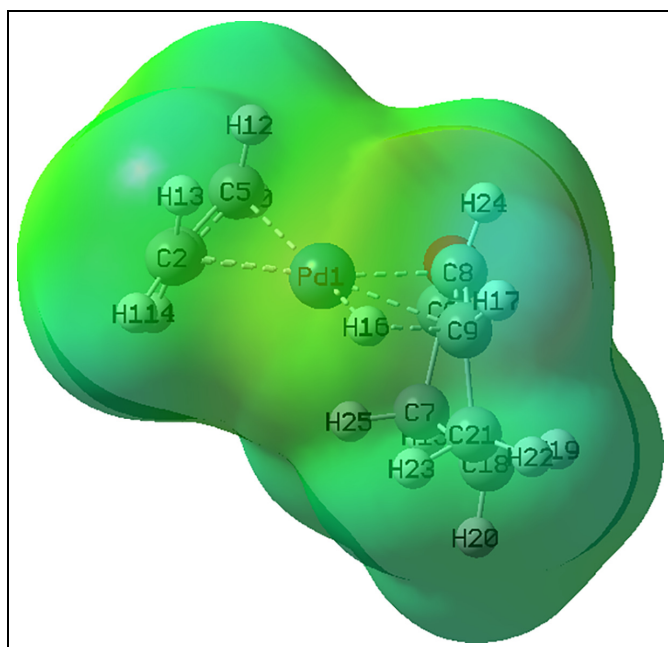


**Figure 8.** The electrostatic potential map of the **TS<sub>BC</sub>** (range =  $-7.160 \text{ e}^{-2} \text{ au}$  (red) to  $+7.160 \text{ e}^{-2} \text{ au}$  (blue); isoval = 0.0004).

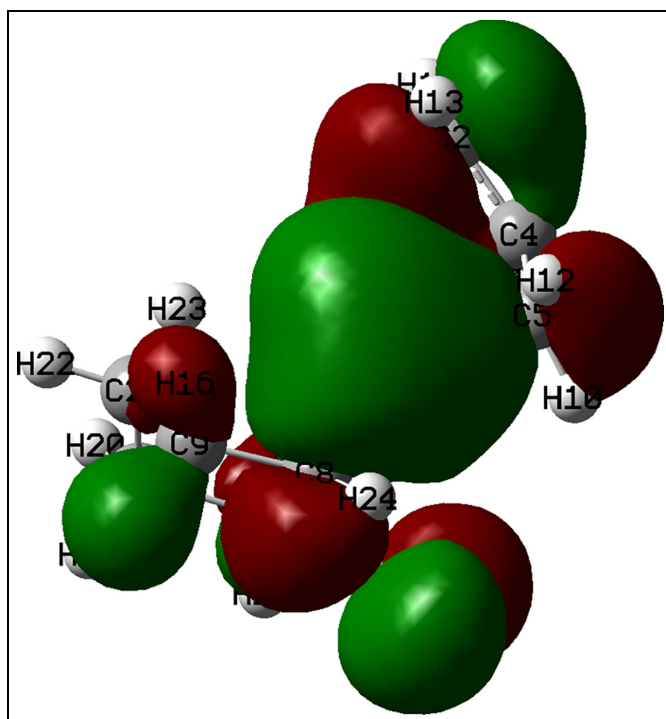


**Figure 9.** The HOMO orbital of complex **B**.

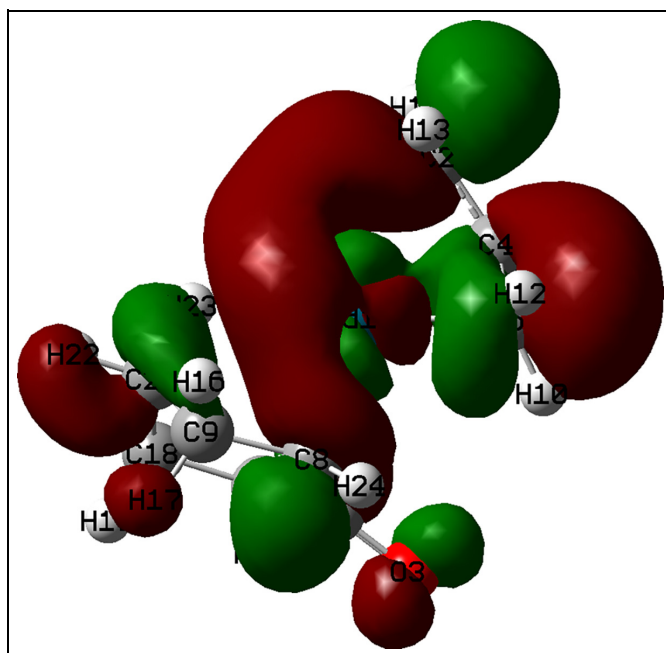


**Figure 10.** The LUMO orbital of complex **B**.

can lead to better control of the reaction conditions and to the development of more efficient catalysts for the dehydrogenation reaction. Hence, further study and experimental results would be desirable in order to reinforce this work.


### Declaration of conflicting interests

The author(s) declared no potential conflicts of interest with respect to the research, authorship, and/or publication of this article.

### Funding

The author(s) received no financial support for the research, authorship, and/or publication of this article.

### ORCID iD

Anan Haj Ichia Arisha  <https://orcid.org/0000-0003-4943-1808>

### Supplemental material

Supplemental material for this article is available online.

### References

1. Shimizu I and Tsuji J. *J Am Chem Soc* 1982; 104: 5846–5847.
2. Shimizu I, Minami I and Tsuji J. *Tetrahedron Lett* 1983; 24: 1797–1800.
3. Tsuji J, Minami I and Shimizu I. *Tetrahedron Lett* 1983; 24: 5636–5638.
4. Tsuji J, Minami I and Shimizu I. *Tetrahedron Lett* 1983; 24: 5639–5640.
5. Minami I, Takahashi K, Shimizu I, et al. *Tetrahedron* 1986; 42: 2971–2977.
6. Muzart J. *Eur J Org Chem* 2010; 3779–3790.
7. Huang D, Zhao Y and Newhouse TR. *Org Lett* 2018; 20: 684–687.
8. Wang Y, Wang M, Li Y, et al. *Chem* 2020; 7: 1180–1223.
9. Maity S, Dolui P, Kancherla R, et al. *Chem Sci* 2017; 8: 5181.
10. Baccalini A, Vergura S, Dolui P, et al. *Org Lett* 2019; 21: 8842–8846.
11. Maiti S, Kancherla R, Dhawa U, et al. *ACS Catal* 2016; 6: 5493–5499.
12. Achar TK, Zhang X, Mondal R, et al. *Angew Chem Int Edit* 2019; 58: 10353–10360.
13. Bag S, Surya K, Mondal A, et al. *J Am Chem Soc* 2020; 142: 12453–12466.
14. Mishra NK, Sharma S, Park J, et al. *ACS Catal* 2017; 7: 2821–2847.
15. Shvo Y and Arisha AH. *J Org Chem* 1998; 63: 5640–5642.
16. Keith JA, Behenna DC, Sherden N, et al. *J Am Chem Soc* 2012; 134: 19050–19060.
17. Frisch MJ, Trucks GW, Schlegel HB, et al. *Gaussian 16*. Wallingford, CT: Gaussian, Inc., 2016.
18. Dennington R, Keith TA and Millam JM. *GaussView* (Version 6.0). Shawnee, KS: Semichem Inc., 2016.